

www.acsaem.org Article

# Nickel-Based Two-Electron Redox Shuttle for Dye-Sensitized Solar Cells in Low Light Applications

Ravinder Kaur,<sup>#</sup> Niharika Dalpati,<sup>#</sup> Jared H. Delcamp, and Byron H. Farnum\*



Cite This: ACS Appl. Energy Mater. 2024, 7, 3645-3655



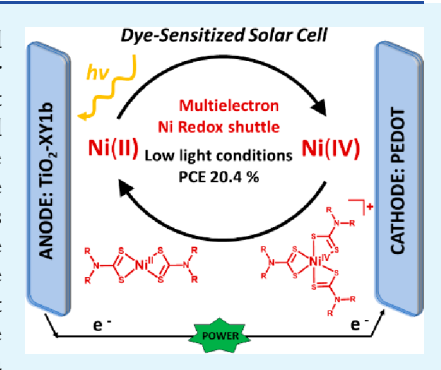
**ACCESS** 

Metrics & More

Article Recommendations

SI Supporting Information

**ABSTRACT:** Dye-sensitized solar cells (DSCs) are important to indoor solar powered devices and energy sustainable buildings because of their remarkable performance under indoor/ambient light conditions. Triiodide/iodide ( $I_3^-/I^-$ ) has been used as the most common redox mediator in DSCs because of its desirable kinetic properties and multielectron redox cycle. However, the low redox potential, corrosiveness, competitive visible light absorption, and lack of tunability of this redox mediator limit its performance in many DSC devices. Here we report a class of transition metal complex redox shuttles which operate on a similar multielectron redox cycle as  $I_3^-/I^-$  while maintaining desirable kinetics and improving on its limitations. These complexes, nickel dithiocarbamates, were evaluated as redox shuttles in DSCs, which exhibited excellent performance under low light conditions. The recombination behavior of the redox shuttles with electrons in  $TiO_2$ , dye regeneration behavior, and counter electrode electron transfer resistance were studied via



chronoamperometry and electrochemical impedance spectroscopy (EIS). Further, DSC devices were studied with the Ni-based redox shuttles via incident photon-to-current conversion efficiencies (IPCEs) and current–voltage (J-V) curves under varied light intensities. The Ni-based redox shuttles showed up to 20.4% power conversion efficiency under fluorescent illumination, which was higher than  $I_3^-/I^-$ -based devices (13%) at similar electrolyte concentrations. Taken together, these results show that nickel dithiocarbamate redox shuttles have faster rates of dye regeneration than the  $I_3^-/I^-$  shuttle but suffer from faster recombination of photoinjected electrons with oxidized Ni(IV) species, which decrease photovoltages.

KEYWORDS: dye-sensitized solar cells, nickel(IV), redox shuttle, dithiocarbamate, indoor photovoltaic

# **■ INTRODUCTION**

Dye-sensitized solar cells (DSCs) have been of tremendous interest in harvesting solar energy for the past three decades due to their advantageous low cost, modular components, esthetic design characteristics, and high light-to-electrical energy conversion efficiency under diffuse light conditions.  $^{1-7}$  DSCs of the n-type variety are typically composed of mesoporous nanocrystalline  ${\rm TiO_2}$  functionalized with a molecular sensitizer as the photoanode, a redox shuttle (RS) in the electrolyte, and a cathode comprised of a conductive material. The photovoltage produced by the solar cell is equal to the difference in the cathode potential, defined by the potential of the RS  $(E_{\rm redox})$  and the Fermi level of the  ${\rm TiO_2}$  photoanode  $(E_{\rm Fermi})$  under illumination.

Since the introduction of high surface area DSCs by O'Regan and Gratzel, the two-electron (2e<sup>-</sup>) redox couple triiodide/iodide ( $I_3^-/I^-$ ) has been studied as an RS due to its fast dye regeneration kinetics and slow recombination rate with  $TiO_2$  electrons.<sup>7–9</sup> These advantages result from the nature of the multielectron redox cycle between iodide (reduced RS) and triiodide (oxidized RS). Rapid regeneration of the sensitizer occurs via the 1e<sup>-</sup> oxidation of  $I^-$  to  $I_2^{\bullet-}$  at 0.30 V vs  $Fc^{+/0}$  followed by quick conversion of  $I_2^{\bullet-}$  to  $I_3^-$  through disproportionation. Recombination of  $TiO_2(e^-)$  with  $I_3^-$  is

slow and is believed to be the result of the low 1e<sup>-</sup> reduction potential for I<sub>3</sub><sup>-</sup> at -0.98 V vs Fc<sup>+/0</sup>. <sup>11,12</sup> Thus, the rapid formation of a 2e<sup>-</sup> product (I<sub>3</sub><sup>-</sup>) following 1e<sup>-</sup> oxidation of I<sup>-</sup> protects the RS from recombination reactions. <sup>23,24</sup> However, the fixed 2e<sup>-</sup> redox potential of the RS at  $E_{\rm redox} = -0.34$  V vs Fc<sup>+/0</sup> is not ideal for many sensitizers and is closer to the conduction band edge of TiO<sub>2</sub> ( $E_{\rm CB} = -0.5$  V vs NHE<sup>1</sup> (-1.14 V vs Fc<sup>+/0</sup>)<sup>13</sup> in acetonitrile (MeCN)) than other metal-based shuttles, resulting in lower open-circuit voltages ( $V_{\rm OC}$ ). <sup>14–16</sup>

Some research has thus shifted toward employing earthabundant first-row transition metal complexes as the RS because of their stability, availability, and redox tunability through both metal and ligand redox properties. Pecifically, shuttles based on Co(III/II) and Cu(II/I) redox couples have gained popularity due to their large  $V_{\rm OC}$  values. The highest efficiency achieved in a single junction DSC under 1 sun conditions with a cobalt-based

Received: December 21, 2023
Revised: April 1, 2024
Accepted: April 10, 2024
Published: April 18, 2024





a) 
$$\begin{bmatrix} I_3^- + 2e^- \longrightarrow 3 \ I^- \end{bmatrix}$$

$$E_{redox} = -0.34$$

$$I_3^- \longrightarrow 0.98 \qquad 0.30$$

$$Ni^{|V}L_3^+ + 1/2 \ Ni^{|I|} + 2e^- \longrightarrow 3/2 \ Ni^{|I|}L_2$$

$$E_{redox} = -0.02$$

$$Ni^{|V}L_3^+ \longrightarrow Ni^{|I|}L_3$$

$$Ni^{|V}L_3^+ \longrightarrow Ni^{|I|}L_3$$

$$Ni^{|V}L_3^+ \longrightarrow Ni^{|I|}L_3$$

$$Ni^{|V}L_3^+ \longrightarrow Ni^{|I|}L_3$$

$$R = -0.02$$

Figure 1. (a) Latimer diagrams of the  $I_3^-/I^-$  redox couple (top) and the  $[Ni(n-Bu_2dtc)_3]^+/Ni(n-Bu_2dtc)_2$  couple (bottom) where  $L = n-Bu_2dtc^-$ . Potentials shown vs  $Fc^{+/0}$ . (b) Chemical structures of nickel dithiocarbamate complexes discussed here.

electrolyte was reported by Kakiage et al. to be 14.3% for [Co(phen)<sub>3</sub>]<sup>3+/2+</sup>, where phen is 1,10-phenanthroline.<sup>24</sup> The highest efficiency obtained with a copper-based electrolyte under 1 sun irradiation was reported by Ren et al. to be 15.2% for [Cu(tmby)<sub>2</sub>]<sup>2+/+</sup>, where tmby is 4,4′,6,6′-tetramethyl-2,2′-bipyridine.<sup>25</sup> Notably, the same copper-based electrolyte was previously reported by Zhang et al. to yield 34.5% efficiency under ambient light conditions (i.e., fluorescence light sources).<sup>26</sup> The result of higher performance under low light conditions is a general result for DSCs and has brought much attention to the use of these solar cells for indoor applications.

The metal-based shuttles reported thus far operate on  $1e^-$  redox cycles. Here, our focus has been to study metal coordination complexes which not only possess  $E_{\rm redox}$  values larger than that of  $I_3^-/I^-$  but also possess multielectron redox cycles similar to that of  $I_3^-/I^-$  to allow for rapid dye regeneration but slow  ${\rm TiO}_2(e^-)$  recombination.

A Latimer diagram for the I<sub>3</sub><sup>-</sup>/I<sup>-</sup> redox couple in MeCN is shown in Figure 1a where the favored 2e reactivity results from potential inversion of the 1e- redox couples due to chemical bond formation with I- anions upon oxidation. In turn, the I2 - intermediate is unstable and disproportionates with a rate constant of  $k_{\rm disp} = 3 \times 10^9 \, {\rm M}^{-1} \, {\rm s}^{-1}$  and  $\Delta G_{\rm disp} = -(0.30 - 0.98) = -1.3 \, {\rm eV} \, ({\rm eq} \, 1).^{8,9}$  Nickel dithiocarbamate complexes  $(Ni(R_2dtc)_2, R_2dtc^- = dithiocarbamate where R is$ an alkyl group) shown in Figure 1b also operate on a 2e redox cycle resulting from increased chemical bond formation upon oxidation from Ni(II) to Ni(IV). 27-29 A Latimer diagram for the nickel di-n-butyldithiocarbamate redox cycle in MeCN is shown in Figure 1a for comparison with  $I_3^-/I^-$ . A similar diagram for the nickel diethyldithiocarbamate redox cycle can be found in Figure S1. Here, oxidation of Ni<sup>II</sup>(R<sub>2</sub>dtc)<sub>2</sub> to  $[Ni^{III}(R_2dtc)_2]^+$  is followed by chemical bond formation with a third R<sub>2</sub>dtc<sup>-</sup> ligand to generate Ni<sup>III</sup>(R<sub>2</sub>dtc)<sub>3</sub>. Disproportionation of the Ni(III) species into [Ni<sup>IV</sup>(R<sub>2</sub>dtc)<sub>3</sub>]<sup>+</sup> and  $Ni^{II}(R_2dtc)_2$  is highly favored (eq 2), much like in the  $I_3^-/I^$ couple. The overall  $2e^- Ni(IV/II)$  redox couples for R = nbutyl and ethyl are  $E_{\rm redox} = -0.02$  and 0.02 V vs Fc<sup>+/0</sup>, respectively. 27-29

$$I_2^{\bullet -} + I_2^{\bullet -} \to I_3^{-} + I^{-} \quad \Delta G_{\text{disp}} = -1.3 \text{ eV}$$
 (1)

$$\mathrm{Ni^{III}L_3} + \mathrm{Ni^{III}L_2}^+ \rightarrow \mathrm{Ni^{IV}L_3}^+ + \mathrm{Ni^{II}L_2} \, \mathrm{L} = n\text{-Bu}_2 \mathrm{dtc}^-$$
  
$$\Delta G_{\mathrm{disp}} = -0.56 \; \mathrm{eV} \tag{2}$$

Based on the Latimer diagrams in Figure 1a, regeneration and recombination reactions in DSCs using a nickel dithiocarbamate redox shuttle would be expected to occur via 1e<sup>-</sup> pathways (eqs 3–4), while the overall photovoltage would be determined by the difference in the 2e<sup>-</sup>  $E_{\rm redox}$  value for the RS and  $E_{\rm Fermi}$  of the TiO<sub>2</sub> photoanode. The  $E_{\rm redox}$  values for the nickel dithiocarbamate shuttles are ~0.3 V greater than  $I_3^-/I^-$  and comparable to  $[{\rm Co(bpy)_3}]^{3+/2+}$  (-0.04 V vs Fc<sup>+/0</sup>), thus a larger photovoltage could be achieved in operational DSCs. <sup>14</sup>

$$TiO_2(e^-)I-S^+ + Ni^{II}(R_2dtc)_2 \rightarrow TiO_2(e^-)I$$
  
-S +  $[Ni^{III}(R_2dtc)_2]^+$  Regeneration (3)

$$\begin{aligned} \text{TiO}_2(\text{e}^-) \text{l-S} + [\text{Ni}^{\text{IV}}(\text{R}_2\text{dtc})_3]^+ &\rightarrow \text{TiO}_2 \text{l-S} + \text{Ni}^{\text{III}} \\ (\text{R}_2\text{dtc})_3 \quad \text{Recombination} \end{aligned} \tag{4}$$

Herein, we report the photoelectrochemical study of [Ni(n- $Bu_2dtc)_3$ ]+/Ni(n- $Bu_2dtc)_2$  (Ni<sub>Bu</sub>+/0) and [Ni(Et<sub>2</sub>dtc)<sub>3</sub>]+/Ni- $(Et_2dtc)_2$   $(Ni_{Et}^{+/0})$  shuttles that operate in a similar fashion as the  $I_3^-/I^-$  couple. While these are not the first redox shuttles to employ nickel metal centers,  $^{30}$  these are the first to employ a multielectron redox cycle with a transition metal. We show that by using these shuttles in DSCs a maximum 20.4% power conversion efficiency (PCE) is obtained under fluorescent light conditions with Ni $_{\rm Bu}^{+/0}$  (4.2% PCE for Ni $_{\rm Et}^{+/0}$ ), compared with 13.0% PCE for  $I_3^{-}/I^{-}$  at similar electrolyte concentrations. Further comparisons with I<sub>3</sub><sup>-</sup>/I<sup>-</sup> show that the nickel-based shuttles displayed faster rates of dye regeneration than I<sub>3</sub><sup>-</sup>/I<sup>-</sup> but suffer from rapid recombination with TiO<sub>2</sub>(e<sup>-</sup>), greatly reducing the measured  $V_{\rm OC}$  values with respect to the maximum theoretical estimates. Striking similarities in the redox chemistry and photochemistry of I<sub>3</sub><sup>-</sup>/I<sup>-</sup> and nickel dithiocarbamate shuttles are further discussed, in addition to advantages and limitations of this new class of RS.

# EXPERIMENTAL SECTION

**General Considerations.** All chemicals were used as received, unless otherwise described. <sup>1</sup>H NMR experiments were performed

with a Bruker 600 MHz instrument. UV—vis absorbance spectroscopy was performed with an Agilent Cary 8454 photodiode array spectrophotometer. Mass spectrometry analyses were performed on a Thermo Fisher Explorus 120 quadrupole orbitrap mass spectrometer with electrospray ionization (ESI) in positive mode using Xcalibur software, where samples were injected into 95% acetonitrile and 5% water for transport to the ESI.

**Synthesis and Characterization.** Bis(*N*,*N*-diethyldithiocarbamate) nickel(II) (Ni(Et<sub>2</sub>dtc)<sub>2</sub>, TCI, >97%) and bis(*N*,*N*-di-*n*-butyldithiocarbamate) nickel(II) (Ni(*n*-Bu<sub>2</sub>dtc)<sub>2</sub>, TCI, > 97%) were purchased and recrystallized by slow evaporation from dichloromethane (DCM, BDH, ACS grade) before use. Characterization of the green solids was performed by <sup>1</sup>H NMR and UV–vis (Figures S2–S3 and S7).  $Ni(Et_2dtc)_2$ : <sup>1</sup>H NMR in acetonitrile-*d*<sub>3</sub> (MeCN-*d*<sub>3</sub>, Cambridge Isotope Laboratories): δ 3.60 (q, –CH<sub>2</sub>–), 1.21 (t, –CH<sub>3</sub>). UV–vis in MeCN (BDH, HiSolv):  $\lambda_{max}(\varepsilon)$  = 388 nm (5,600 M<sup>-1</sup> cm<sup>-1</sup>).  $Ni(n\text{-}Bu_2dtc)_2$ : <sup>1</sup>H NMR in MeCN-*d*<sub>3</sub>: δ 3.53 (t, –CH<sub>2</sub>–), 1.60 (quin, –CH<sub>2</sub>), 1.31 (sext, –CH<sub>2</sub>–), 0.92 (t, –CH<sub>3</sub>). UV–vis in MeCN:  $\lambda_{max}(\varepsilon)$  = 388 nm (6,200 M<sup>-1</sup> cm<sup>-1</sup>). Both solids were kept in a vacuum oven (VWR) at least 2 days before use.

Oxidized nickel complexes were synthesized using a modified previously reported literature.  $^{28,31}$  [Ni(R<sub>2</sub>dtc)<sub>3</sub>]BF<sub>4</sub>, where R = ethyl or *n*-butyl, was synthesized by oxidizing Ni(R<sub>2</sub>dtc)<sub>2</sub> with ~1.3 equiv of nitrosonium tetrafluoroborate (NOBF<sub>4</sub>, BTC, 98%) in DCM. Solutions for both complexes turned dark red-brown and were kept stirring for 3 h, followed by filtration and solvent evaporation to yield a reddish brown solid (>80% yield). [Ni(Et<sub>2</sub>dtc)<sub>3</sub>]BF<sub>4</sub>:  $^{1}$ H NMR (Figure S4) in DCM- $^{4}$ 2:  $\delta$  3.66 (q,  $^{-}$ CH<sub>2</sub> $^{-}$ ), 1.32 (t,  $^{-}$ CH<sub>3</sub>). UV-vis in MeCN (Figure S7):  $\lambda_{\text{max}}$  ( $\varepsilon$ ) = 437 nm (10,300 M $^{-1}$  cm $^{-1}$ ). ESI-MS: m/z for [NiC<sub>15</sub>H<sub>30</sub>N<sub>3</sub>S<sub>6</sub>] $^{+}$ : 502.0112 (found), 502.0117 (calc). [Ni( $^{-}$ Bu<sub>2</sub>dtc)<sub>3</sub>]BF<sub>4</sub>:  $^{1}$ H NMR (Figure S5) in MeCN- $^{4}$ 3:  $\delta$  3.60 (t,  $^{-}$ CH<sub>2</sub> $^{-}$ ), 1.66 (quin,  $^{-}$ CH<sub>2</sub>), 1.36 (sext,  $^{-}$ CH<sub>2</sub> $^{-}$ ), 0.94 (t,  $^{-}$ CH<sub>3</sub>). UV-vis in MeCN (Figure S7):  $\lambda_{\text{max}}$  = 435 nm (8,400 M $^{-1}$  cm $^{-1}$ ). ESI-MS (Figure S6): m/z for [NiC<sub>27</sub>H<sub>54</sub>N<sub>3</sub>S<sub>6</sub>] $^{+}$ : 670.1983 (found), 670.1995 (calc).

DSC Fabrication. DSC devices were prepared as previously described in the literature. 32 Chenodeoxycholic acid (CDCA, Chem-Impex International), sensitizing dye XY1b ((E)-3-(4-(6-(7-(4-(bis(2',4'-dibutoxy-[1,1'-biphenyl]-4-yl) amino) phenyl) benzo[c]-[1,2,5]thiadiazol-4-yl)-4,4-bis(2-ethylhexyl)-4*H*-cyclopenta[2,1-b:3,4b']dithiophen-2-yl) phenyl)-2-cyanoacrylic acid, Dyenamo), and solvents (ethanol, chloroform, MeCN, Sigma-Aldrich) were purchased and used as received. TEC 10 and TEC 7 FTO glass (Hartford Glass) were used for the photoanode and counter electrode, respectively. The electrolyte components 4-tert-butylpyridine (TBP) and lithium bis(trifluoromethanesulfonyl)imide (LiTFSI) were purchased from Ambeed. The iodine (I2, crystalline) used in the DSC electrolytes was purchased from Alfa Aesar. 1,3-Dimethylimidazolium iodide (DMII) was purchased from IOLITEC Ionic liquids technologies. The photoanode consisted of a 4 µm mesoporous TiO<sub>2</sub> active layer (30 nm particle size, 30NR-D, Greatcell Solar) and a 4  $\mu$ m TiO<sub>2</sub> scattering layer (>100 nm particle size, Solaronix R/SP). The working photoanode was prepared by immersing the TiO<sub>2</sub> film (0.38 cm<sup>2</sup>) into an XY1b dye solution for 18 h. The solution used for dye dipping/sensitizing was prepared by using a concentration of 0.1 mM XY1b dye in an EtOH:CHCl<sub>3</sub> (9:1) solution with 2.5 mM CDCA. PEDOT (poly(3,4-ethylenedioxythiophene)) counter electrodes were prepared following the literature procedure with some minor changes and utilized for all devices in this study.<sup>33</sup> Predrilled TEC 7 FTO glass was washed with 0.1 M HCl solution in ethanol and then washed with acetone and sonicated in acetone for 10 min. The glass was then dried at 400 °C for 15 min, left to cool, and then cut into pieces of 2 cm  $\times$  2 cm. The solution for electropolymerization contained a micellar aqueous solution of 0.1 M SDS (sodium dodecyl sulfate, Thermo Scientific, >99% purity) and 0.01 M EDOT (3,4-ethylenedioxythiophene, Sigma-Aldrich) obtained by dissolving the SDS and EDOT in deionized water and sonicating for 60 min. Electropolymerization of EDOT was performed with a C-H Instruments electrochemical analyzer Model CHI602E with a two-electrode cell consisting of a 2

cm  $\times$  2 cm FTO glass counter electrode and the predrilled 2 cm  $\times$  2 cm FTO glass described above as the working electrode. A constant current of 2.75 mA was applied for 110 s to obtain the polymerized PEDOT film. The resulting PEDOT electrode was then washed with DI water, dried with air, and then dried further on a hot plate at 140 °C for 2 min. The same procedure was used to prepared PEDOT as working electrodes in cyclic voltammetry (CV) experiments except TEC 7 glass cut into 0.5 cm  $\times$  2 cm electrodes rather than 2 cm  $\times$  2 cm. The active area used in the CV experiment for the PEDOT working electrode was 0.1 cm² where excess PEDOT was removed by wiping the electrode surface with a DI water-soaked Kim wipe (Kimtech) to leave only the active area intact.

Three different electrolytes were prepared for DSC studies according to the following mixtures: (1) 30 mM Ni(Et<sub>2</sub>dtc)<sub>2</sub>, 15 mM [Ni(Et<sub>2</sub>dtc)<sub>3</sub>]<sup>+</sup>, 0.5 M TBP (4-tert-butylpyridine), and 0.1 M LiTFSI (lithium bis(trifluoromethanesulfonyl)imide) in MeCN; (2) 30 mM Ni $(n-Bu_2dtc)_2$ , 15 mM [Ni<sup>IV</sup> $(n-Bu_2dtc)_3$ ]<sup>+</sup>, 0.5 M TBP, and 0.1 M LiTFSI in MeCN; (3) 30 mM 1,3-dimethylimidazolium iodide (DMII), 15 mM I<sub>2</sub>, 0.5 M TBP, and 0.1 M LiTFSI in MeCN. Note that Ni(Et<sub>2</sub>dtc)<sub>2</sub> has limited solubility in MeCN (about 5 mM), thus the electrolyte was used after syringe filtration to give a solution saturated in a metal complex. Additionally, devices were also fabricated with 4-trifloromethyl-pyridine (TFMP) in  $\mathrm{Ni_{Bu}}^{+/0}$  RS instead of TBP in RS, while keeping all other components of the RS the same. The photoanode and cathode were sealed with a 25  $\mu$ m thick hot melt film (Surlyn, DuPont) by heating the counter electrode at 130 °C under 0.15 psi pressure for 55 s. Devices were completed by filling the cells with electrolyte through the predrilled holes in the counter electrodes, and the holes were sealed with a Surlyn precut circle and a thin glass cover by heating at 130 °C under 0.1 psi for 25

DSC Device Characterization. DSC cell measurements were conducted as previously reported.32 J-V curves were generated utilizing masked solar cells with a circular active area of 0.15 cm<sup>2</sup>. Photovoltaic characteristics were measured using a 300 W xenon lamp (Model SF300A, SCIENCETECH Inc. Class AAA) solar simulator equipped with an AM 1.5 G filter for less than 2% spectral mismatch. Prior to each measurement, the solar simulator output was calibrated with a KG5 filtered monocrystalline silicon NREL calibrated reference cell from ABET Technologies (Model 15150-KG5). The current density-voltage characteristic of each cell was obtained with a Keithley digital source meter (Model 2400). The incident photon-tocurrent conversion efficiency (IPCE) was measured with an IPCE instrument manufactured by Dyenamo comprising a 175 W xenon lamp (CERMAX, Model LX175F), a monochromator (Spectral Products, Model CM110, Czerny-Turner, dual grating), a filter wheel (Spectral Products, Model AB301T, fitted with filter AB3044 [440 nm high pass] and filter AB3051 [510 nm high pass]), a calibrated UV-enhanced silicon photodiode reference, and Dyenamo issued

Indoor/ambient lighting characterization was performed by I-Vanalysis using an Osram 011318-L36W/930 fluorescent tube as the illumination source. An irradiance spectrum of this light source has been reported previously in the literature.<sup>2</sup> The light intensity was determined prior to each measurement using a digital lux meter (Model LX1330B, Dr. Meter) in combination with a solar power meter (Solar-100) and varied by changing the distance between the light source and the device under study. We note that conversion between lux and mW/cm<sup>2</sup> units for light intensity is highly dependent on the light source. Thus, our measurement of both values prior to each experiment avoids any confusion in data conversion. Data for the J-V plots for devices measured at 1370, 4660, and 10000 lx under fluorescent lighting was collected with a Keithley 2400 source meter and SweepMe! software (version 1.5.5), taking data points every 20 mV with an ~15 s equilibration time allowed between each data point collected. The potential range scanned was determined for each device by first measuring the device voltage with a Fluke 87 V Max multimeter to limit the reverse direction current at higher applied voltages. Scans in the forward and reverse directions overlay without any signs of hysteresis at this scan rate (1.3 mV/s).

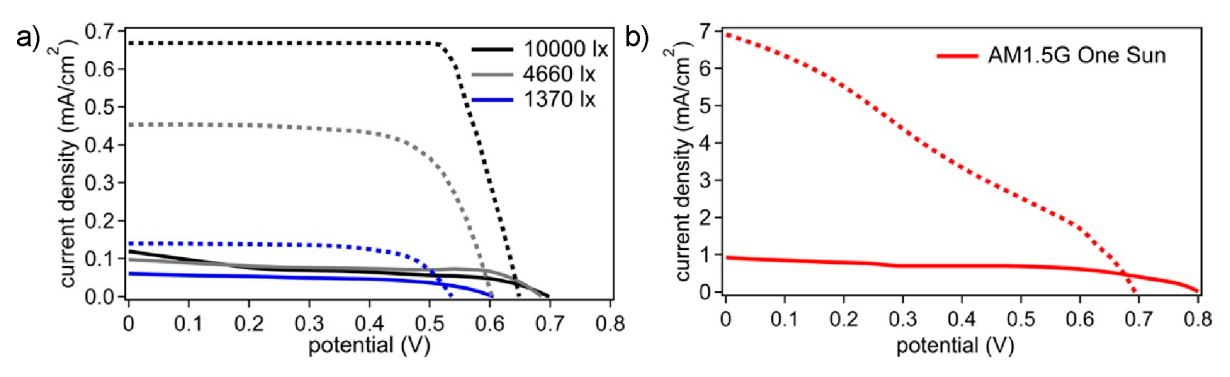


Figure 2. J-V curves of DSCs with redox mediators  $Ni_{Et}^{+/0}$  (solid lines) and  $Ni_{Bu}^{+/0}$  (dashed lines) under fluorescent (a) and solar simulated light sources (b).

Table 1. Summary of DSC Device Performance Metrics

Fluorescent Light										
Incident Power lx (mW/cm²)	RS	$V_{ m OC}~({ m mV})$	$J_{SC}$ (mA/cm <sup>2</sup> )	FF (%)	PCE (%)					
1,370 (0.30)	$^{a}$ Ni $_{Bu}$ $^{+/0}$	$563 \pm 18$	$0.13 \pm 0.01$	69 ± 4	$17.3 \pm 0.9$					
	$^{b}\mathrm{Ni_{Et}}^{+/0}$	$590 \pm 14$	$0.07 \pm 0.01$	$49 \pm 3$	$7.0 \pm 0.3$					
	$^{c}I_{3}^{-}/I^{-}$	$584 \pm 18$	$0.10 \pm 0.02$	$72 \pm 0$	$13.1 \pm 2.7$					
4,660 (0.93)	$\mathrm{Ni_{Bu}}^{+/0}$	$614 \pm 9$	$0.46 \pm 0.01$	$68 \pm 0$	$20.4 \pm 0.1$					
	$\mathrm{Ni_{Et}}^{+/0}$	$676 \pm 20$	$0.12 \pm 0.04$	$69 \pm 13$	$4.0 \pm 0.2$					
	$I_3^-/I^-$	$632 \pm 25$	$0.31 \pm 0.05$	$66 \pm 5$	$13.5 \pm 0.7$					
10,000 (2.02)	$\mathrm{Ni_{Bu}}^{+/0}$	$651 \pm 3$	$0.67 \pm 0.00$	$83 \pm 3$	$17.8 \pm 0.7$					
	$\mathrm{Ni_{Et}}^{+/0}$	$690 \pm 14$	$0.18 \pm 0.08$	$35 \pm 11$	$1.4 \pm 0.1$					
	$I_3^-/I^-$	$650 \pm 13$	$0.67 \pm 0.00$	$63 \pm 1$	$13.6 \pm 0.6$					
Solar Simulated Light										
Incident Power (mW/cm <sup>2</sup> )	RS	$V_{ m OC}~({ m mV})$	$J_{SC}$ (mA/cm <sup>2</sup> )	FF (%)	PCE (%)					
100	$\mathrm{Ni_{Bu}}^{+/0}$	$776 \pm 14$	$6.27 \pm 0.31$	24 ± 1	$1.2 \pm 0.1$					
	$\mathrm{Ni_{Et}}^{+/0}$	$756 \pm 40$	$0.80 \pm 0.14$	$52 \pm 2$	$0.3 \pm 0.1$					
	$I_3^-/I^-$	$593 \pm 19$	$4.64 \pm 0.70$	$67 \pm 7$	$1.8 \pm 0.2$					

"Prepared electrolyte concentrations:  $Ni_{Bu}^{+/0}$ : 15 mM [Ni(n-Bu<sub>2</sub>dtc)<sub>3</sub>]<sup>+</sup>, 30 mM Ni(n-Bu<sub>2</sub>dtc)<sub>2</sub>.  $^bNi_{Et}^{+/0}$ : 15 mM [Ni(Et<sub>2</sub>dtc)<sub>3</sub>]<sup>+</sup>, 30 mM Ni(Et<sub>2</sub>dtc)<sub>2</sub>.  $^cI_3^-/I^-$ : 15 mM I<sub>2</sub>, 30 mM DMII. All electrolytes contained 0.1 M LiTFSI in MeCN with 0.5 M TBP. \*Values are the average of at least two DSC devices.

Constant illumination electrochemical impedance spectroscopy (EIS) was measured by using a potentiostat (CHI 6054E with frequency analyzer) with an applied bias equal to the  $V_{\rm OC}$  obtained through J-V measurements. The DSC devices were illuminated using a fluorescent or solar simulated (AM1.5 G) light source as indicated. The spectra were scanned in the frequency range 10<sup>-1</sup>-10<sup>5</sup> Hz at room temperature. The alternating current (AC) amplitude was set at 10 mV. The EIS model circuit fitting data was obtained from the software feature provided with the CH-Instruments potentiostat.  $V_{\rm OC}$ decay experiments were carried out with a Dyenamo Toolbox (DN-AE01) instrument with a white LED light source. By placing neutral density filters in front of the LED, three light intensities, 0.3 mW/cm<sup>2</sup> (1370 lx), 0.93 mW/cm<sup>2</sup> (4660 lx), and 2.02 mW/cm<sup>2</sup> (10000 lx), were studied. For 1 sun illumination, a light intensity of 100 mW/cm<sup>2</sup> was used from a 300 W xenon lamp (Model SF300A, SCIENCETECH Inc. Class AAA) solar simulator equipped with an AM 1.5 G filter for a less than 2% spectral mismatch.

Photoelectrochemistry. A photoelectrochemical cell (Gamry Instruments, Figure S8) was used to measure the photocurrent versus time data. This cell consisted of a cylindrical chamber (12 mm diameter × 30 mm length) with open ports for reference (Ag/AgCl, Gamry) and counter electrodes (Pt wire, BASi) and O-ring sealed front and back face plates. The front face plate contained a 12 mm diameter circular hole through which light was able to pass into the photoelectrochemical cell. A dye-sensitized TiO<sub>2</sub> photoanode deposited on conductive FTO glass (SnO<sub>2</sub>:F, 15 ohm/cm², Hartford Glass, Inc.) was pressed against metal contacts embedded in the body of the photoelectrochemical cell and sandwiched from the backside

using the front face plate and four screws. Metal contacts were connected internally to designated connection ports on top of the photoelectrochemical cell such that the photoanode could be connected as the working electrode in a three-electrode setup. A white light LED (ThorLabs, MWWHL4) was used for illumination.

The  ${\rm TiO_2}$  photoanode used for these studies was produced from  ${\rm TiO_2}$  nanoparticles synthesized by an established procedure.  $^{34}$   ${\rm TiO_2}$  nanoparticles were then doctor bladed onto FTO glass by using a single layer of Scotch tape to define the film thickness and annealed in a box furnace (Thermofisher Scientific) at 450 °C for 30 min. Films were cut into square pieces according to the size required by the photoelectrochemical cell, and the dye was loaded for 15–20 h with XY1b dye in a 9:1 ethanol:DCM solvent mixture.

Electrolytes were comprised of a 1.5 mM reduced nickel complex and 1 mM oxidized nickel complex in MeCN with 0.1 M TBAPF<sub>6</sub>. Reduced electrolytes contain only a 1.5 mM Ni(II) complex or TBAI in 0.1 M TBAPF<sub>6</sub>. The iodide source was TBAI (tetrabutylammonium iodide from Merck, >98%). Triiodide/iodide ( $I_3^-/I^-$ ) was obtained after reacting 2.5 M tetrabutylammonium iodide with 0.25 M iodine (Sigma-Aldrich, >99.99%) in MeCN at room temperature and then diluting to the required concentration before use.

Photoinduced chronoamperometry was conducted using Gamry potentiostats 1010E and 1010B. The LED was connected to the Gamry 1010E, whereas the photoelectrochemical cell was connected to the Gamry 1010B. Five different light conditions were used: 0 (dark), 10, 30, 50, 70, and 100 mW/cm<sup>2</sup>.

Dark Electrochemistry. Cyclic voltammetry data using PEDOT working electrodes were measured with a CH Instruments electro-

chemical analyzer Model CHI602E. The working electrode was PEDOT deposited on FTO glass; the pseudoreference electrode was Ag/AgCl; and the counter electrode was platinum wire. The supporting electrolyte was 0.1 M LiTFSI in MeCN with and without the addition of 0.5 M TBP. Ten mM Ni(Bu<sub>2</sub>dtc)<sub>2</sub> was used; however, due to the solubility limit of Ni(Etdtc)<sub>2</sub>, a saturated solution of Ni(Etdtc)<sub>2</sub> was used. All measurements were conducted under an argon atmosphere at a scan rate of 50 mV/s. Ferrocenium/ferrocene was used as a reference standard with oxidation and reduction potentials of the materials reported versus  $Fc^{+/0}$  in MeCN.

#### RESULTS AND DISCUSSION

DSC devices were fabricated with either nickel- or iodinebased electrolytes for comparison. The devices were assembled with a TiO<sub>2</sub> photoanode sensitized with the commercially available XY1b dye and a PEDOT counter electrode. This sensitizer was selected due to its wider spectral response and well-established use for efficient electricity generation under low light and full sun conditions. The photoanode consisted of a 4  $\mu$ m mesoporous TiO<sub>2</sub> active layer film thickness comprised of 30 nm particles which provides increased porosity for improved mass transport of the electrolyte relative to 20 nm particles.  $^{36-38}$  An additional 4.0  $\mu$ m TiO<sub>2</sub> scattering layer (>100 nm particles) was used to increase the light-harvesting efficiency in the DSC device. 39,40 The devices were characterized by current density versus voltage (J-V) analysis for determination of the PCE given by the equation: PCE =  $(J_{SC} \times V_{OC} \times FF)/I_0$ , where  $V_{OC}$  is opencircuit voltage,  $J_{SC}$  the short-circuit current density, FF the fill factor, and Io the incident light intensity. Devices were investigated under three fluorescent light intensities, 0.3  $mW/cm^2$  (1,370 lx), 0.93  $mW/cm^2$  (4,660 lx), and 2.02 mW/cm<sup>2</sup> (10,000 lx), and a solar simulated spectrum at AM 1.5G (100 mW/cm<sup>2</sup>). Figure 2 shows a summary of J-Vcurves obtained from these studies, while Table 1 provides a summary of performance metrics. Dark *I*–*V* curves are shown in Figure S9.

At 1,370 lx fluorescent illumination, the Ni<sub>Bu</sub> +/0 RS-based DSC devices reached a PCE of 17.3%. The observed PCE corresponded to a device output power ( $P_{\rm out}$ ) of 51.9  $\mu \rm W/cm^2$ , a  $V_{\rm OC}$  of 563 mV,  $J_{\rm SC}$  of 0.13 mA/cm², and a FF of 70%. Increasing the intensity of the incident fluorescent lighting to 4,660 lx resulted in a higher PCE of 20.4% with a  $P_{\rm out}$  of 189.7  $\mu W/\text{cm}^2$ ,  $V_{OC}$  of 620 mV,  $J_{SC}$  of 0.46 mA/cm<sup>2</sup>, and FF of 67%. A further increase in light intensity to 10,000 lx resulted in a decrease of PCE to 17.5%. The initial PCE decreased less than 10% after 1 h of continuous illumination under fluorescent lighting (Table S1), indicating the DSC devices were relatively stable under the conditions measured here. Further I-Vanalysis under solar simulated light (AM 1.5G, 100 mW/cm<sup>2</sup>) showed a  $V_{\rm OC}$  of 776 mV,  $J_{\rm SC}$  of 6.27 mA/cm<sup>2</sup>, and FF of 24% for an overall PCE of 1.2%. The  $\mathrm{Ni_{Et}}^{+/0}$  RS followed the same trend as  $\mathrm{Ni_{Bu}}^{+/0}$  in terms of  $V_{\mathrm{OC}}$  and  $J_{\mathrm{SC}}$  but with much lower values for  $J_{\mathrm{SC}}$ , and a maximum PCE of 7.0% was observed at 1,370 lx. The PCE observed under solar simulated illumination with  $Ni_{Et}^{+/0}$  was poor at 0.3%. Notably,  $Ni(Et_2dtc)_2$  has significant solubility limitations in MeCN (≤5 mM) which could lead to depletion of the reduced shuttle at the TiO<sub>2</sub>sensitizer interface under higher light intensities, resulting in a low regeneration efficiency. Thus, only the  ${\rm Ni_{Bu}}^{+/0}$ -based devices were further studied for incident photon-to-current efficiency (IPCE) and electrochemical impedance spectroscopy (EIS) with a focus on fluorescent (low light intensity) conditions.

The nickel-based devices were directly compared with devices prepared using  $I_3^-/I^-$  as the redox shuttle. Note that in these devices the concentration of  $I_3^-/I^-$  was decreased from its typically high millimolar range to match the concentrations used for the nickel shuttle. In terms of photocurrent,  $J_{SC}$  values for  $I_3^-/I^-$  devices were lower than those for  $Ni_{Bu}^{+/0}$  RS devices but higher than those for  $Ni_{Et}^{+/0}$  DSC devices were likely due to the limited solubility of  $Ni(Et_2dtc)_2$  in MeCN, concentration differences between  $I^-$  and  $Ni(n-Bu_2dtc)_2$  may also explain the greater  $J_{SC}$  values for  $Ni_{Bu}^{+/0}$ . For example, the initial concentration of  $[Ni(n-Bu_2dtc)_2]$  at 30 mM is expected to be the same for the final electrolyte solution; however, the equilibrium of  $I^-$  with  $I_2$  to produce  $I_3^-$  reduces the initial  $[I^-]$  from 30 to 15 mM once the electrolyte is fully prepared. The photocurrent results were corroborated with IPCE measurements (Figure 3) which showed maximums

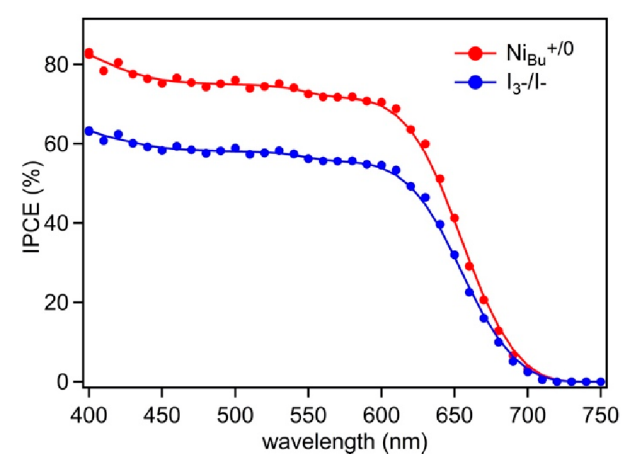


Figure 3. IPCE spectra recorded for  ${\rm Ni_{Bu}}^{+/0}$  RS (red) and  ${\rm I_3}^-/{\rm I}^-$  RS (blue) based DSC devices.

of 82% for  $\mathrm{Ni_{Bu}}^{+/0}$  and 63% for  $\mathrm{I_3}^-/\mathrm{I}^-$ . These data suggest that the  $\mathrm{Ni_{Bu}}^{+/0}$  RS offers competitive rates with traditional iodine-based RS for regeneration. It is important to note that the IPCE spectrum here is generated via a direct current measurement as is common in the DSC field which is under inherently low photon flux conditions.

Under low light conditions, the iodine-based devices reported similar  $V_{\rm OC}$  values as nickel-based devices, ranging from 610 to 659 mV. The maximum theoretical photovoltage (V<sub>OC</sub> max) for DSC devices is approximated as the energetic difference between the semiconductor (TiO<sub>2</sub>) conduction band and the redox potential of the RS defined by the Nernst equation. Although the conduction band can shift with electrolyte salts and additives, the TiO2 CB is commonly approximated at  $E_{\rm CB} = -0.5$  V vs NHE in the DSC literature. This value can be converted to the Fc<sup>+/0</sup> reference by the subtraction of -0.64 V to result in  $E_{\rm CB}$  =  $-1.14 \text{ V vs Fc}^{+/0}$  in MeCN. <sup>13,44</sup> Comparison of this value with the standard two-electron  $E_{\text{redox}}$  values for nickel-based and iodine-based shuttles given in Figure 1a results in  $V_{\rm OC}^{\rm max}$  = 1120, 1160, and 800 mV for Ni<sub>Bu</sub> +/0, Ni<sub>Et</sub> +/0, and  $I_3$  -/I RS devices. This shows that the iodine-based devices yielded  $V_{\rm OC}$ s closer to the theoretical maximum ( $\sim$ 160 mV below  $V_{\rm OC}^{\rm max}$ ) than nickel-based devices (>460 mV below  $V_{\rm OC}^{\rm max}$ ). Overall, the PCE for iodine-based devices was lower than with  ${\rm Ni_{Bu}}^{+/0}$ -based devices under low light conditions, and the  ${\rm Ni_{Bu}}^{+/0}$  RS

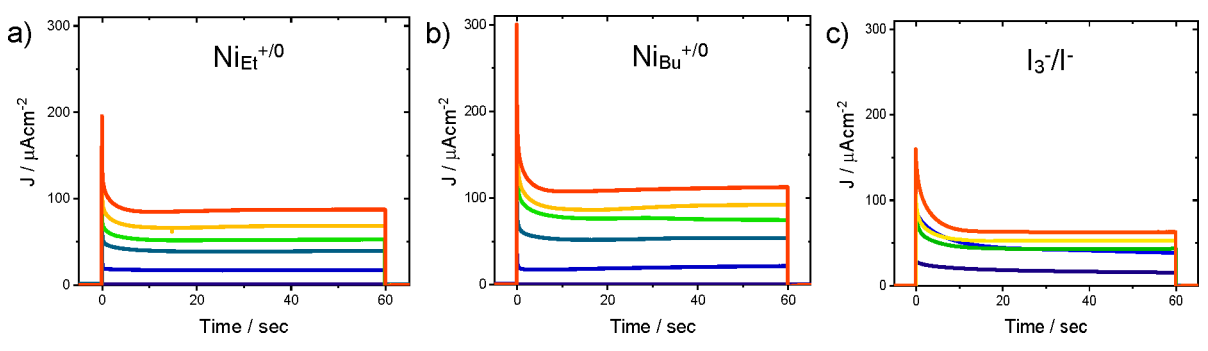


Figure 4. Chronoamperometry data collected with five different intensities (0, 10, 30, 50, 70, and 100 mW/cm²) from an LED source using a photoelectrochemical cell (PCE) containing different RS combinations. (a)  $\mathrm{Ni_{Et}}^{+/0}\left(E_{\mathrm{app}}=-0.09~\mathrm{V}~\mathrm{vs}~\mathrm{Fc}^{+/0}\right)$ , (b)  $\mathrm{Ni_{Bu}}^{+/0}\left(E_{\mathrm{app}}=-0.09~\mathrm{V}~\mathrm{ys}~\mathrm{fc}^{-/0}\right)$ , (b)  $\mathrm{Ni_{Bu}}^{+/0}\left(E_{\mathrm{app}}=-0.09~\mathrm{V}~\mathrm{ys}~\mathrm{fc}^{-/0}\right)$ , (c)  $\mathrm{I_3}^{-}/\mathrm{I^{-}}\left(E_{\mathrm{app}}=-0.14~\mathrm{V}~\mathrm{y}\right)$ . In all experiments, the concentration of the reduced shuttle was 1.5 mM, and the oxidized shuttle was 1 mM in MeCN with a 0.1 M TBAPF<sub>6</sub> electrolyte. The working electrode was a mesoporous nanocrystalline  $\mathrm{TiO_2}$  photoanode sensitized with XY1b; the counter electrode was a Pt wire; and the reference electrode was Ag/AgCl.

shuttle exhibited maximum performance at 4,660 lx with a PCE of 20.4%. To the best of our knowledge, values this high under ambient light conditions with a nickel-based RS have not been achieved yet in the DSC field. However, cosensitization of XY1b with other photosensitizers has achieved record PCE values of 34.5% with a Cu-based RS and 36% when using a Co-based RS. 5,23 Under solar simulated conditions, the iodine-based device PCE surpassed the Ni<sub>Bu</sub> +/0 RS-based device PCE, 1.9% versus 1.2%, respectively. The higher PCE with iodine is due to a lower FF (24% vs 61%) for  $\mathrm{Ni_{Bu}}^{+/0}$  despite the larger  $V_{\mathrm{OC}}$  and  $J_{\mathrm{SC}}$  with nickel-based devices. The low FF might be attributed to the slow mass transport as both the oxidized and reduced complexes of the nickel-based RS could be subjected to mass-transport limitation due to bulky groups on the dithiocarbamate ligand, while for I<sub>3</sub><sup>-</sup>/I<sup>-</sup>-based electrolytes, diffusion restrictions on the current arise only for the triiodide ions. 45-47 The low FF may also be due to a low recombination resistance at the TiO<sub>2</sub>redox interface as compared to I<sub>3</sub><sup>-</sup>/I<sup>-</sup> RS, leading to a rapid back reaction of photoinjected electrons with the oxidized redox species as discussed below in regeneration studies and in EIS data (Figure 4 and Table 2).

**Regeneration.** To further examine the dye regeneration capabilities of the  $Ni_{Bu}^{+/0}$  and  $Ni_{Et}^{+/0}$  shuttles with  $I_3^-/I^-$ , controlled photoelectrochemical studies were performed outside the DSC construct to eliminate any factors related to

Table 2. Summary of EIS Data for DSCs with  $Ni_{Bu}^{+/0}$  or  $I_3^-/I^-$  Electrolytes<sup>a</sup>

Fluorescent Light										
RS	$R_{ ext{CE}} \ (\Omega)$	$C_{\mathrm{CE}} \ (\mu\mathrm{F})$	$R_{ m rec} \ (\Omega)$	$C_{\mu} (\mu F)$	$ au_{ m rec} ( m ms)$					
$\mathrm{Ni_{Bu}}^{+/0}$	58	13.5	2472	65	161					
$I_3^-/I^-$	101	7.2	4078	138	563					
$\mathrm{Ni_{Bu}}^{+/0}$	32	23.9	927	94	87					
$I_3^-/I^-$	71	8.8	1741	153	266					
$\mathrm{Ni_{Bu}}^{+/0}$	22	72.6	493	144	71					
$I_3^-/I^-$	82	8.5	841	189	159					
Solar Simulated Light										
RS	$R_{ ext{CE}} \ (\Omega)$	$C_{CE} (\mu F)$	$R_{ m rec} \ (\Omega)$	$\binom{C_{\mu}}{(\mu \mathrm{F})}$	$ au_{ m rec} \ ( m ms)$					
$\mathrm{Ni_{Bu}}^{+/0}$	22	0.2	366	567	208					
$I_3^-/I^-$	66	7.9	162	214	35					
	$\begin{array}{c} \text{RS} \\ \text{Ni}_{\text{Bu}}^{}+/0} \\ \text{I}_{3}^{}}/\Gamma \\ \text{Ni}_{\text{Bu}}^{}+/0} \\ \text{I}_{3}^{}}/\Gamma \\ \text{Ni}_{\text{Bu}}^{}+/0} \\ \text{I}_{3}^{}}/\Gamma \\ \text{Solar} \\ \end{array}$	$\begin{array}{c c} RS & R_{CE} \\ Ni_{Bu}^{+/0} & 58 \\ I_3^{}/\Gamma & 101 \\ Ni_{Bu}^{+/0} & 32 \\ I_3^{}/\Gamma & 71 \\ Ni_{Bu}^{+/0} & 22 \\ I_3^{}/\Gamma & 82 \\ \hline Solar Simulate \\ RS & (\Omega) \\ Ni_{Bu}^{} & 22 \\ \end{array}$	$\begin{array}{c ccccccccccccccccccccccccccccccccccc$	$\begin{array}{c ccccccccccccccccccccccccccccccccccc$	$\begin{array}{c ccccccccccccccccccccccccccccccccccc$					

<sup>&</sup>lt;sup>a</sup>DSC active area of 0.15 cm<sup>2</sup>.

the PEDOT cathode or solution resistance. Photoinduced chronoamperometry experiments were performed using a photoelectrochemical cell (PEC) as described in the Experimental Section. The PEC was assembled as a threeelectrode system where the working electrode consisted of a nanocrystalline TiO2 film sensitized with XY1b, the reference electrode was Ag/AgCl, and the counter electrode was a Pt wire. For a direct comparison between nickel mediators and  $I_3^-/I^-$ , the concentrations of Ni<sup>II</sup>(R<sub>2</sub>dtc)<sub>2</sub> and I<sup>-</sup> were set to 1.5 mM, while  $[Ni(R_2dtc)_3]^+$  and  $I_3^-$  were set to 1 mM. As discussed above for the DSC measurements, the solubility of Ni(Et<sub>2</sub>dtc)<sub>2</sub> is only 5 mM in MeCN solution. Therefore, a lower concentration of 1.5 mM was chosen to ensure that all of the mediator species were completely dissolved. The ratio of 3:2 reduced:oxidized mediator was chosen to match the balanced stoichiometry of the  $2e^-$  redox reaction for the nickel mediators (Figure 1a). In the case of  $Ni_{Et}^{+/0}$  and  $Ni_{Bu}^{+/0}$ , 0.5 mM  $Ni^{II}(ClO_4)_2$  was also added to balance the redox reaction.

In these experiments, a constant voltage was applied to the sensitized  $TiO_2$  photoanode near  $E_{redox}$  for each mediator, to simulate the short-circuit condition of a DSC device, while the resulting current was measured as a function of 5 different light intensities ranging from 0 mW/cm<sup>2</sup> to 100 mW/cm<sup>2</sup> (Figure 4). For all three mediators, the photocurrent density was observed to spike when the light was initially turned on before settling to constant values within 10 s. This spike was observed to be the largest for  $Ni_{Bu}^{+/0}$  and the smallest for  $I_3^-/I^-$ . Likewise, the magnitude of the drop in the photocurrent from the spike to the constant value at longer times was also largest for  $Ni_{Bu}^{+/0}$  and smallest for  $I_3^-/I^-$ . The spikes in photocurrent reflect initial fast dye regeneration capabilities, which are higher for the nickel-based shuttles compared with iodide; however, the large drops in photocurrent observed for these mediators are the result of depletion of the reduced shuttle at the TiO2 surface, which may be attributed to slow mass transport, leading to rapid recombination of TiO<sub>2</sub>(e<sup>-</sup>) with oxidized shuttles in the solution.

Despite the drop in the photocurrent density, the steady-state values were larger for nickel mediators than for  $I_3^-/I^-$ . A plot of photocurrent density obtained at 50 s for each RS as a function of light intensity is shown in Figure 5. In all cases, the photocurrent density increased with light intensity, as expected, but began to level off at higher irradiances. This is attributed to the low concentrations of the reduced shuttle present in solution (1.5 mM). At higher light intensities, more

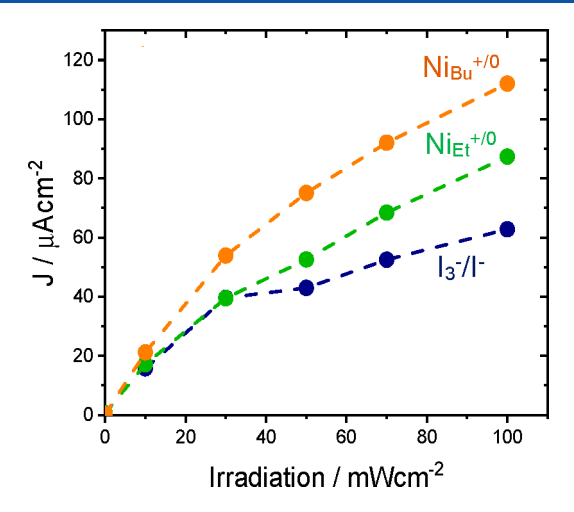


**Figure 5.** Comparison of photocurrent density versus irradiance plot for all three redox shuttles obtained from photoelectrochemical cell measurements. Photocurrent densities were taken from Figure 4 at 50 s. Orange:  $Ni_{Bu}^{+/0}$ . Green:  $Ni_{Et}^{+/0}$ . Blue:  $I_3^-/I^-$ .

excited-state molecules are generated, and more electrons are injected into TiO<sub>2</sub>. However, the dye regeneration rate at these low concentrations of RS may not be sufficient to keep up with the higher photon flux. If all internal processes, such as electron injection, electron transport through TiO2, and dye regeneration, are sufficiently fast so that light absorption is the rate-limiting step, then a linear relationship would be observed between photocurrent density and light intensity, with the slope of the line being equal to the combined efficiencies for the internal processes. However, if photocurrent density is independent of irradiance (nonlinear), a rate-limiting step other than light absorption is in control. Assuming that electron injection and electron transport are not rate limiting due to each measurement being performed with TiO2/XY1b electrodes and the applied potential being near the shortcircuit condition, the differences in photocurrent at high irradiance are ascribed to differences in dye regeneration efficiencies. Although photocurrent densities did not completely plateau in Figure 5, we can infer that the dye regeneration rate must increase in the order  $I_3^-/I^- < Ni_{Et}^{+/0}$ < Ni<sub>Bu</sub> +/0 based on the order of photocurrent density at 100  $mW/cm^2$ .

**Recombination.** The difference of >460 mV in the  $V_{\rm OC}$  of DSC devices with  $\mathrm{Ni_{Bu}}^{+/0}$  and  $\mathrm{Ni_{Et}}^{+/0}$  with respect to their  $V_{\mathrm{OC}}^{\mathrm{max}}$  suggests rapid recombination between  $\mathrm{TiO_2}(\mathrm{e^-})$  and oxidized RS species. Based on the large  $\Delta G_{
m disp}$  for Ni(III) complexes in the redox cycle (eq 2), we presume that recombination with  $[Ni^{IV}(R_2dtc)_3]^+$  is the most likely pathway (eq 4). Electrochemical impedance spectroscopy (EIS) studies were performed on operational DSCs to quantify the lifetime associated with the recombination  $(\tau_{rec})$  of  $TiO_2(e^-)$  to [Ni<sup>IV</sup>(R<sub>2</sub>dtc)<sub>3</sub>]<sup>+</sup>. Specifically, comparative EIS experiments were conducted with the  $Ni_{Bu}^{+/0}$  RS and  $I_3^{-}/I^{-}$  RS-based DSC devices at open-circuit potential bias to probe electron transfer resistances and recombination electron lifetimes. These experiments were also conducted under constant illumination with different light intensities (100 mW/cm<sup>2</sup>), 2.02 mW/cm<sup>2</sup>, 0.93 mW/cm<sup>2</sup>, and 0.3 mW/cm<sup>2</sup>) produced by using neutral density filters in front of an LED light source.

The Nyquist plots (Figure S10) consisted of two semicircles, the smaller of which represents the electrolyte–counter electrode interface ( $R_{CE}|C_{CE}$ ). The larger semicircle represents

the  ${\rm TiO_2}$ –electrolyte interface and thus gives information on the resistance associated with recombination ( $R_{\rm rec}$ ) of electrons from the  ${\rm TiO_2}$  CB with the electrolyte. These two assignments are consistent with constant illumination EIS results for DSC devices. The recombination lifetime for electrons in  ${\rm TiO_2}$  was then calculated according to the equation  $\tau_{\rm rec} = R_{\rm rec} C_{\mu\nu}$  where  $C_{\mu}$  is the capacitance at the  ${\rm TiO_2}$ –electrolyte interface measured by EIS. Table 2 provides a summary of fitting constants used to describe the EIS results. The corresponding circuit model can be found in Figure S11 and represents a series of two parallel RIC circuits and is common for DSC devices.

Under fluorescent light conditions,  $R_{\rm rec}$  and  $\tau_{\rm rec}$  for  $I_3^-/I^-$  devices were found to be larger than those of  ${\rm Ni_{Bu}}^{+/0}$  devices, indicating slower recombination of electrons in  ${\rm TiO_2}$  with  $I_3^-$  than  ${\rm Ni_{Bu}}^+$ . For both electrolytes under fluorescent lighting, the maximum  $\tau_{\rm rec}$  was achieved at the lowest light intensity, with values of 563 ms for  $I_3^-/I^-$  and 161 ms for  ${\rm Ni_{Bu}}^{+/0}$ . Such high electron lifetimes in  ${\rm TiO_2}$  contribute significantly to the efficient performance of DSC devices under low light conditions.

High recombination resistance (long  $\tau_{\rm rec}$ ) between injected electrons in the metal oxide and the dye/RS is known to lead to an increase in  $V_{\rm OC}$  for DSC devices. The longer  $\tau_{\rm rec}$  observed for  $I_3^-/I^-$  devices is thus correlated with these devices having  $V_{\rm OC}$  values closer to the  $V_{\rm OC}^{\rm max}$  values compared with Ni<sub>Bu</sub>+/0 devices (Table 1). The higher recombination resistance of iodine-based devices can be further explained by an energy level diagram (Figure 6).

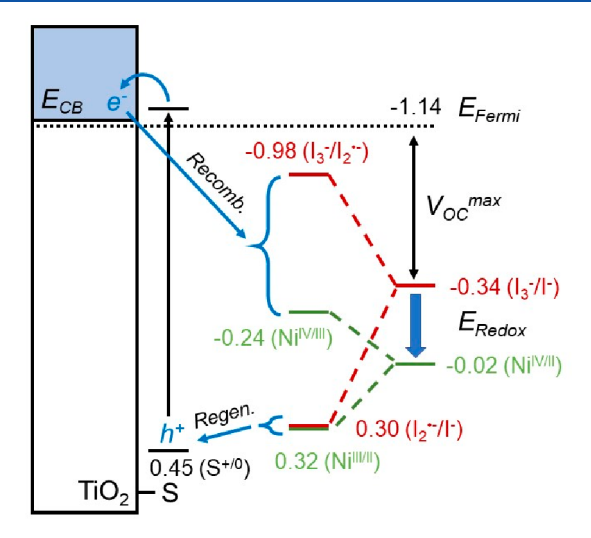


**Figure 6.** Comparison of  $1e^-$  and  $2e^-$  redox potentials for the  $I_3^-/I^-$  RS and the Ni<sub>Bu</sub><sup>+/0</sup> RS in relation to their function within a DSC. Redox potentials are referenced to Fc<sup>+/0</sup>.

Here, the driving force for recombination ( $\Delta G_{\rm rec}$ ) from the TiO<sub>2</sub> CB (E<sub>CB</sub>) to I<sub>3</sub><sup>-</sup> (I<sub>3</sub><sup>-</sup>/I<sub>2</sub><sup>•</sup>-) is much lower than that to Ni<sub>Bu</sub><sup>+</sup> (Ni<sup>IV/III</sup>), eqs 5 and 6. This also helps explain why the nickel-based RS devices exhibited much smaller  $V_{\rm OC}$  values in comparison to their theoretical maximums.

$$TiO_2(e^-) + I_3^- \to TiO_2 + I_2^{\bullet -} + I^-$$
  
 $\Delta G_{rec} = -0.16 \text{ eV}$  (5)

$$\operatorname{TiO}_{2}(e^{-}) + \left[\operatorname{Ni}^{\text{IV}}(n-\operatorname{Bu}_{2}\operatorname{dtc})_{3}\right]^{+} \to \operatorname{TiO}_{2} + \operatorname{Ni}^{\text{III}}$$

$$(n-\operatorname{Bu}_{2}\operatorname{dtc})_{3} \quad \Delta G_{\text{rec}} = -0.90 \text{ eV}$$
(6)

Surprisingly,  $R_{\rm rec}$  and  $au_{\rm rec}$  were found to be larger for  ${\rm Ni_{Bu}}^{+/0}$ than for I<sub>3</sub><sup>-</sup>/I<sup>-</sup> under solar simulated lighting conditions. This result is also correlated with DSC device performance in Table 1 where the  $Ni_{Bu}^{+/0}$  RS achieved a higher  $V_{OC}$  value than  $I_3^-/$  $I^-$ . This result may be due to photodecomposition of  $Ni_{Bu}^{\phantom{Bu}}$ under higher light intensities, first reported by Fackler in 1973, thus removing the oxidized redox shuttle needed for recombination. 50 Equation 7 shows the reported photodecomposition reaction by Fackler which results in Ni<sup>II</sup>(R<sub>2</sub>dtc)<sub>2</sub>, Ni(II) ions, and the corresponding thiuram disulfide  $(R_2dtc)_2$ . The conversion of  $[Ni(R_2dtc)_3]^+$  into Ni(R<sub>2</sub>dtc)<sub>2</sub> was corroborated by our photodecomposition experiments shown in Figure S12 for [Ni(Et<sub>2</sub>dtc)<sub>3</sub>]<sup>+</sup>. If photodecomposition were to occur, the ultimate oxidized product would be thiuram disulfide, which may not be as easily reduced as [Ni(R<sub>2</sub>dtc)<sub>3</sub>]<sup>+</sup>, thus resulting in a slower recombination lifetime. Notably,  $I_3^-$  is also known to photodecompose according to eq 8. 51,52 However, when  $I_3^$ is in MeCN solution with a high concentration of I<sup>-</sup>, the iodine atoms (I $^{\bullet}$ ) are rapidly converted to  $I_2^{\bullet-}$  ( $K_{eq} = 6 \times 10^6 \text{ M}^{-1}$ ) followed by disproportionation of  $I_2^{\bullet-}$  back to  $I_3^-$  according to eq 1.<sup>51</sup> Thus, the concentration of  $I_3^-$  in the  $I_3^-/I^-$  electrolyte mixture is not expected to decrease significantly under constant illumination. In the case of [Ni<sup>IV</sup>(R<sub>2</sub>dtc<sub>3</sub>)]<sup>+</sup>, photodecomposition is reversible in MeCN but occurs on a slow time scale under dark conditions.50

$$2[Ni^{IV}(R_2dtc)_3]^+ + h\nu$$

$$\rightarrow Ni^{II}(R_2dtc)_2 + Ni^{II} + 2(R_2dtc)_2$$
 (7)

$$I_3^- + h\nu \to I_2^{\bullet -} + I^{\bullet} \tag{8}$$

The implications of the photodecomposition of  $[Ni^{IV}(R_2dtc)_3]^+$  are important to the understanding of the nickel mediator's function within the solar cell. First, it is unclear what the steady-state concentration of [Ni<sup>IV</sup>(R<sub>2</sub>dtc)<sub>3</sub>]<sup>+</sup> is under constant illumination. While pure solutions of [Ni<sup>IV</sup>(R<sub>2</sub>dtc)<sub>3</sub>]<sup>+</sup> may bleach under strong visible light (Figure S12), the extent to which these molecules can absorb light within a DSC is unclear. Namely, there are sensitizer molecules designed to harvest visible photons and thus serve as competitive light absorbers. DSCs measured in this study were also illuminated through the FTOlTiO<sub>2</sub> side, as is typical for the field, in order to maximize the light absorption by sensitizer molecules. Given the photosensitivity of  $[Ni^{1V}(R_2dtc)_3]^+$ , it is plausible that higher irradiances could yield a greater light absorption by these molecules and thus alter the composition of the redox shuttle. Further studies in this regard and the extent to which thiuram disulfide plays a role in the redox shuttle are currently under investigation.

**Impact of TBP on Redox Cycle.** The addition of *tert*-butylpyridine (TBP) is essential to most n-type DSCs employing  $\text{TiO}_2$  photoanodes. TBP is believed to both raise the conduction band energy of  $\text{TiO}_2$  to give higher  $E_{\text{Fermi}}$  values and block the approach of oxidized redox shuttles to the  $\text{TiO}_2$  surface which increases charge recombination lifetimes and open-circuit voltages. However, many redox shuttles based on transition metal complexes have noted coordination of TBP to the metal center, thus producing a deleterious effect on the redox cycle of the RS.  $^{54-58}$ 

The impact of pyridine coordination on the Ni<sub>Et</sub><sup>+/0</sup> shuttle has already been investigated in detail by our group using electrochemical methods with glassy carbon working electrodes.<sup>27,29</sup> These studies found that coordination of pyridines to the nickel center occurs upon oxidation from Ni<sup>II</sup>(Et<sub>2</sub>dtc)<sub>2</sub> to [NiIII(Et2dtc)2]+, forming both monopyridine  $[Ni^{III}(Et_2dtc)_2(py)]^+$  and bispyridine  $[Ni^{III}(Et_2dtc)_2(py)_2]^+$ complexes. The ratio of mono- vs bispyridine complexes was determined by the  $pK_a$  of the pyridine, with TBP resulting in an ~20:80 ratio for mono:bis complexes. Importantly, the coordination of pyridine in the intermediate Ni(III) oxidation state shifted the Ni(III/II) redox potential in the negative direction. In the study presented here, this negative shift would increase the driving force for dye regeneration. Figure S13 shows experimental evidence of this anodic peak shift for Ni<sub>Bu</sub> and Ni<sub>Et</sub> oxidation in the form of cyclic voltammetry data using a PEDOT working electrode. In the case of  ${\rm Ni_{Bu}}^+$ ,  $E_{\rm pa}$  shifted from 0.26 V vs Fc<sup>+/0</sup> to 0.02 V (–240 mV shift). In the case of  $Ni_{Et}^+$ ,  $E_{va}$  shifted from 0.26 to -0.04 V (-300 mV shift).

Our previously reported electrochemical studies further showed that despite pyridine coordination  $[Ni^{IV}(Et_2dtc)_3]^+$  is still produced, indicating that pyridine coordination only alters the pathway for the redox cycle, but not the end result. 27,29 Figure S13 confirms this observation for the case of a PEDOT working electrode where the cathodic peaks associated with the reduction of  ${\rm Ni_{Bu}}^+$  ( $E_{\rm pc}$  = -0.34 V) and  ${\rm Ni_{Et}}^+$  ( $E_{\rm pc}$  = -0.31 V) are still observed in the presence of TBP and are virtually unchanged in their peak positions. Given the shift in the Ni(III/II) potential, the overall 2e<sup>-</sup> redox potentials for Ni<sub>Ft</sub> +/0 and  $Ni_{Bu}^{+/0}$  are also shifted in the presence of TBP. Taking  $E_{1/2} = (E_{pc} - E_{pa})/2$  obtained from the data in Figure S13 as an approximation for  $E_{\text{redox}}$  of each nickel complex,  $E_{1/2}$  shifts from -0.04 to -0.16 V (-120 mV shift) for  $\mathrm{Ni_{Bu}}^{+/0}$  and from -0.03 to -0.18 V (-150 mV shift) for Ni<sub>Et</sub><sup>+/0</sup>. Such shifts in the  $E_{\rm redox}$  values in a negative direction in the presence of TBP certainly factor into the lower-than-expected  $V_{\rm OC}$  values with respect to the  $V_{\rm OC}^{\rm max}$ .

Despite the fact that the nickel-based shuttles are affected by TBP coordination, comparative testing with a TBP alternative trifluoromethylpyridine (TFMP) using the Ni<sub>Bu</sub><sup>+/0</sup> RS indicates that the inclusion of TBP in the electrolyte is essential to producing the highest solar energy conversion efficiency. Table S3 provides a summary of this comparative DSC data where the  $J_{SC}$  values for  $\mathrm{Ni_{Bu}}^{+/0}$  with TBP vs TFMP were the same; however, the  $V_{\rm OC}$  obtained from TBP devices was >2× larger than that obtained from TFMP devices. Lower V<sub>OC</sub> values with TFMP-based devices are expected relative to devices having TBP in electrolyte.<sup>59</sup> Ndaleh et al. have shown that TFMP in the electrolyte lowers the  $V_{\rm OC}$  and increases the  $J_{SC}$  values (for sensitizers with injection challenges) in the DSC devices due to an increase in electron injection efficiency of the device by shifting the conduction band energy of TiO2 more positive relative to the conduction band energy of TiO2 in the presence of TBP. 54,59 Furthermore, Figure S14 and Table S4 show that recombination lifetimes were >3× longer for TBP electrolytes compared with TFMP electrolytes. Changes in recombination lifetime and  $V_{\rm OC}$  between TBP and TFMP point to differences in the interaction between these species and the TiO2 surface and not to changes in the redox cycle of the nickel-based RS, based on the fact that the Ni<sub>Bu</sub>(IV/III) potential is unaffected by the presence of TBP. Switching between TBP and TFMP almost certainly causes changes in the  $Ni_{Bu}(III/II)$  potential; however, the consistency in  $J_{SC}$ 

values between the different DSCs shows that these changes in potential do not hinder the ability of the redox shuttle to perform dye regeneration.

# CONCLUSION

Here we have studied two nickel-based redox shuttles, Ni<sub>Bu</sub> +/0 and Ni<sub>Et</sub> +/0, for use in DSCs. These shuttles possess redox cycles similar to that of the popular and effective  $I_3^-/I^-$  redox couple. Specifically, they are able to regenerate oxidized dye molecules via 1e redox chemistry (i.e., Ni(III/II) and I<sub>2</sub>•-/I<sup>-</sup>) but quickly convert to 2e<sup>-</sup> products (Ni(IV) and I<sub>3</sub><sup>-</sup>) through disproportionation of radical intermediates. Photocurrentphotovoltage data from solar cell studies showed the highest PCE obtained for the  $Ni_{Bu}^{+/0}$  shuttle at 20.4% under diffuse light conditions (4,660 lx), whereas  $Ni_{Et}^{+/0}$  showed 4.2% under the same lighting conditions. The decreased performance in the Ni<sub>Et</sub> +/0 RS is ascribed to its limited solubility in MeCN. While many examples of transition-metal-based redox shuttles have employed 1e<sup>-</sup> redox cycles, these redox shuttles make use of multielectron redox cycles similar to  $I_3^-/I^-$ . Comparative studies with I<sub>3</sub><sup>-</sup>/I<sup>-</sup> under similar electrolyte concentrations with  ${\rm Ni_{Bu}}^{+/0}$  and  ${\rm Ni_{Et}}^{+/0}$  show that the nickel-based shuttles outperformed  ${\rm I_3}^-/{\rm I}^-$  in terms of dye regeneration. However, recombination of TiO<sub>2</sub>(e<sup>-</sup>) with oxidized Ni(IV) complexes proved to be much faster than recombination with I<sub>3</sub>, with this difference being attributed to the large driving force for recombination of Ni(IV) complexes. Given the versatility in ligand synthesis of the dithiocarbamate framework, nickel dithiocarbamate redox shuttles could provide new avenues for improving the performance of DSCs under diffuse lighting conditions. Current objectives are focused on improving the solubility of the Ni(R<sub>2</sub>dtc)<sub>2</sub> complexes and limiting interactions of  $[Ni(R_2dtc)_3]^+$  with the  $TiO_2$  surface through installation of sterically bulky R groups.

# ASSOCIATED CONTENT

# Supporting Information

The Supporting Information is available free of charge at https://pubs.acs.org/doi/10.1021/acsaem.3c03198.

<sup>1</sup>H NMR, ESI-MS, Nyquist plots, and tables of DSC and EIS data (PDF)

# AUTHOR INFORMATION

# **Corresponding Author**

Byron H. Farnum — Department of Chemistry and
Biochemistry, Auburn University, Auburn, Alabama 36830,
United States; orcid.org/0000-0001-9152-1909;
Email: farnum@auburn.edu

# **Authors**

Ravinder Kaur – Department of Chemistry, University of Mississippi, University, Mississippi 38677, United States; orcid.org/0000-0002-9394-4451

Niharika Dalpati – Department of Chemistry and Biochemistry, Auburn University, Auburn, Alabama 36830, United States

Jared H. Delcamp — Department of Chemistry, University of Mississippi, University, Mississippi 38677, United States; Air Force Research Laboratory, Materials and Manufacturing Directorate (RXNC), Wright-Patterson AFB, Ohio 45433, United States; orcid.org/0000-0001-5313-4078

Complete contact information is available at:

# https://pubs.acs.org/10.1021/acsaem.3c03198

### **Author Contributions**

\*R.K. and N.D. contributed equally.

#### Notes

The authors declare no competing financial interest.

#### ACKNOWLEDGMENTS

First and foremost, we acknowledge the loss of coauthor and graduate student Niharika Dalpati who passed away during the writing of this manuscript. We are forever grateful to have known her. N.D. and B.H.F. acknowledge support from the National Science Foundation through a CAREER award CHE-1945160. R.K. and J.H.D. thank the National Science Foundation for supporting this work through NSF grant CHE-1954922.

#### REFERENCES

- (1) Hagfeldt, A.; Boschloo, G.; Sun, L.; Kloo, L.; Pettersson, H. Dye-Sensitized Solar Cells. *Chem. Rev.* **2010**, *110*, 6595–6663.
- (2) Freitag, M.; Teuscher, J.; Saygili, Y.; Zhang, X.; Giordano, F.; Liska, P.; Hua, J.; Zakeeruddin, S. M.; Moser, J.-E.; Grätzel, M.; Hagfeldt, A. Dye-Sensitized Solar Cells for Efficient Power Generation under Ambient Lighting. *Nat. Photonics* **2017**, *11* (6), 372–378.
- (3) Liu, Y.; Cao, Y.; Zhang, W.; Stojanovic, M.; Dar, M. I.; Péchy, P.; Saygili, Y.; Hagfeldt, A.; Zakeeruddin, S. M.; Grätzel, M. Electron-Affinity-Triggered Variations on the Optical and Electrical Properties of Dye Molecules Enabling Highly Efficient Dye-Sensitized Solar Cells. *Angew. Chem., Int. Ed.* **2018**, *57* (43), 14125–14128.
- (4) Fakharuddin, A.; Jose, R.; Brown, T. M.; Fabregat-Santiago, F.; Bisquert, J. A Perspective on the Production of Dye-Sensitized Solar Modules. *Energy Environ. Sci.* **2014**, *7* (12), 3952–3981.
- (5) Venkatesan, S.; Hsu, T.-H.; Teng, H.; Lee, Y.-L. Dye-Sensitized Solar Cells with Efficiency over 36% under Ambient Light Achieved by Cosensitized Tandem Structure. *Sol. RRL* **2023**, 7 (11), 2300220.
- (6) Muñoz-García, A. B.; Benesperi, I.; Boschloo, G.; Concepcion, J. J.; Delcamp, J. H.; Gibson, E. A.; Meyer, G. J.; Pavone, M.; Pettersson, H.; Hagfeldt, A.; Freitag, M. Dye-Sensitized Solar Cells Strike Back. *Chem. Soc. Rev.* **2021**, *50* (22), 12450–12550.
- (7) O'Regan, B.; Gratzel, M. A Low-Cost, High-Efficiency Solar Cell Based on Dye-Sensitized Colloidal TiO2 Films. *Nature* **1991**, *353*, 737–740.
- (8) Boschloo, G.; Hagfeldt, A. Characteristics of the Iodide/Triiodide Redox Mediator in Dye-Sensitized Solar Cells. *Acc. Chem. Res.* **2009**, 42 (11), 1819–1826.
- (9) Rowley, J. G.; Farnum, B. H.; Ardo, S.; Meyer, G. J. Iodide Chemistry in Dye-Sensitized Solar Cells: Making and Breaking I-I Bonds for Solar Energy Conversion. *J. Phys. Chem. Lett.* **2010**, *1* (20), 3132–3140.
- (10) Farnum, B. H.; Jou, J. J.; Meyer, G. J. Visible Light Generation of I-I Bonds by Ru-Tris(Diimine) Excited States. *Proc. Natl. Acad. Sci. U. S. A.* **2012**, *109* (39), 15628–15633.
- (11) Farnum, B. H.; Gardner, J. M.; Meyer, G. J. Flash-Quench Technique Employed To Study the One-Electron Reduction of Triiodide in Acetonitrile: Evidence for a Diiodide Reaction Product. *Inorg. Chem.* **2010**, *49* (22), 10223–10225.
- (12) Farnum, B. H.; Ward, W. M.; Meyer, G. J. Flash-Quench Studies on the One-Electron Reduction of Triiodide. *Inorg. Chem.* **2013**, 52 (2), 840–847.
- (13) Pavlishchuk, V. V.; Addison, A. W. Conversion Constants for Redox Potentials Measured versus Different Reference Electrodes in Acetonitrile Solutions at 25° C. *Inorg. Chim. Acta* **2000**, 298, 97–102.
- (14) Hamann, T. W. The End of Iodide? Cobalt Complex Redox Shuttles in DSSCs. Dalton Trans. 2012, 41 (11), 3111.
- (15) Yanagida, S.; Yu, Y.; Manseki, K. Iodine/Iodide-Free Dye-Sensitized Solar Cells. Acc. Chem. Res. 2009, 42 (11), 1827–1838.

- (16) Kirner, J. T.; Elliott, C. M. Are High-Potential Cobalt Tris(Bipyridyl) Complexes Sufficiently Stable to Be Efficient Mediators in Dye-Sensitized Solar Cells? Synthesis, Characterization, and Stability Tests. *J. Phys. Chem. C* **2015**, *119* (31), 17502–17514.
- (17) Dalle, K. E.; Warnan, J.; Leung, J. J.; Reuillard, B.; Karmel, I. S.; Reisner, E. Electro- and Solar-Driven Fuel Synthesis with First Row Transition Metal Complexes. *Chem. Rev.* **2019**, *119* (4), 2752–2875.
- (18) Pashaei, B.; Shahroosvand, H.; Abbasi, P. Transition Metal Complex Redox Shuttles for Dye-Sensitized Solar Cells. *RSC Adv.* **2015**, *5* (115), 94814–94848.
- (19) Hattori, S.; Wada, Y.; Yanagida, S.; Fukuzumi, S. Blue Copper Model Complexes with Distorted Tetragonal Geometry Acting as Effective Electron-Transfer Mediators in Dye-Sensitized Solar Cells. J. Am. Chem. Soc. 2005, 127 (26), 9648–9654.
- (20) Bai, Y.; Yu, Q.; Cai, N.; Wang, Y.; Zhang, M.; Wang, P. High-Efficiency Organic Dye-Sensitized Mesoscopic Solar Cells with a Copper Redox Shuttle. *Chem. Commun.* **2011**, *47* (15), 4376–4378.
- (21) Yella, A.; Lee, H.-W.; Tsao, H. N.; Yi, C.; Chandiran, A. K.; Nazeeruddin, M. K.; Diau, E. W.-G.; Yeh, C.-Y.; Zakeeruddin, S. M.; Grätzel, M. Porphyrin-Sensitized Solar Cells with Cobalt (II/III)-Based Redox Electrolyte Exceed 12% Efficiency. *Science* **2011**, 334 (6056), 629–634.
- (22) Zhou, D.; Yu, Q.; Cai, N.; Bai, Y.; Wang, Y.; Wang, P. Efficient Organic Dye-Sensitized Thin-Film Solar Cells Based on the Tris(1,10-Phenanthroline)Cobalt(II/III) Redox Shuttle. *Energy Environ. Sci.* **2011**, *4* (6), 2030–2034.
- (23) Li, L.; Zhao, L.; Jiang, X.; Yu, Z.; Liu, J.; Rui, H.; Shen, J.; Sharmoukh, W.; Allam, N. K.; Sun, L. Efficient Dye-Sensitized Solar Cells Based on Bioinspired Copper Redox Mediators by Tailoring Counterions. *J. Mater. Chem. A* **2022**, *10* (8), 4131–4136.
- (24) Kakiage, K.; Aoyama, Y.; Yano, T.; Oya, K.; Fujisawa, J.; Hanaya, M. Highly-Efficient Dye-Sensitized Solar Cells with Collaborative Sensitization by Silyl-Anchor and Carboxy-Anchor Dyes. Chem. Commun. 2015, 51 (88), 15894–15897.
- (25) Ren, Y.; Zhang, D.; Suo, J.; Cao, Y.; Eickemeyer, F. T.; Vlachopoulos, N.; Zakeeruddin, S. M.; Hagfeldt, A.; Grätzel, M. Hydroxamic Acid Pre-Adsorption Raises the Efficiency of Cosensitized Solar Cells. *Nature* **2023**, *613* (7942), 60–65.
- (26) Zhang, D.; Stojanovic, M.; Ren, Y.; Cao, Y.; Eickemeyer, F. T.; Socie, E.; Vlachopoulos, N.; Moser, J.-E.; Zakeeruddin, S. M.; Hagfeldt, A.; Grätzel, M. A Molecular Photosensitizer Achieves a Voc of 1.24 V Enabling Highly Efficient and Stable Dye-Sensitized Solar Cells with Copper(II/I)-Based Electrolyte. *Nat. Commun.* 2021, 12 (1), 1777.
- (27) Richburg, C. S.; Farnum, B. H. Influence of Pyridine on the Multielectron Redox Cycle of Nickel Diethyldithiocarbamate. *Inorg. Chem.* **2019**, *58* (22), 15371–15384.
- (28) Mazumder, Md. M. R.; Dalpati, N.; Pokkuluri, P. R.; Farnum, B. H. Zinc-Catalyzed Two-Electron Nickel(IV/II) Redox Couple for Multi-Electron Storage in Redox Flow Batteries. *Inorg. Chem.* **2022**, *61* (48), 19039–19048.
- (29) Mazumder, Md. M. R.; Burton, A.; Richburg, C. S.; Saha, S.; Cronin, B.; Duin, E.; Farnum, B. H. Controlling One-Electron vs Two-Electron Pathways in the Multi-Electron Redox Cycle of Nickel Diethyldithiocarbamate. *Inorg. Chem.* **2021**, *60* (17), 13388–13399.
- (30) Li, T. C.; Spokoyny, A. M.; She, C.; Farha, O. K.; Mirkin, C. A.; Marks, T. J.; Hupp, J. T. Ni(III)/(IV) Bis(Dicarbollide) as a Fast, Noncorrosive Redox Shuttle for Dye-Sensitized Solar Cells. *J. Am. Chem. Soc.* **2010**, *132* (13), 4580–4582.
- (31) Lachenal, D. Electrochemical Behaviour of Nickel (II) and Ni (IV) N,N-Diethyldithiocarbamates. Synthesis of a Nickel(IV) Species. *Inorg. Nucl. Chem. Lett.* **1975**, *11* (2), 101–106.
- (32) Cheema, H.; Delcamp, J. H. SnO2 Transparent Printing Pastes from Powders for Photon Conversion in SnO2-Based Dye-Sensitized Solar Cells. *Chem.—Eur. J.* **2019**, 25 (62), 14205–14213.
- (33) Ellis, H.; Vlachopoulos, N.; Häggman, L.; Perruchot, C.; Jouini, M.; Boschloo, G.; Hagfeldt, A. PEDOT Counter Electrodes for Dye-Sensitized Solar Cells Prepared by Aqueous Micellar Electrodeposition. *Electrochim. Acta* 2013, 107, 45–51.

- (34) Oskam, G.; Bergeron, B. V.; Meyer, G. J.; Searson, P. C. Pseudohalogens for Dye-Sensitized TiO2 Photoelectrochemical Cells. *J. Phys. Chem. B* **2001**, *105* (29), 6867–6873.
- (35) Cao, Y.; Liu, Y.; Zakeeruddin, S. M.; Hagfeldt, A.; Grätzel, M. Direct Contact of Selective Charge Extraction Layers Enables High-Efficiency Molecular Photovoltaics. *Joule* **2018**, 2 (6), 1108–1117.
- (36) Pradhan, S. C.; Velore, J.; Hagfeldt, A.; Soman, S. Probing Photovoltaic Performance in Copper Electrolyte Dye-Sensitized Solar Cells of Variable TiO2 Particle Size Using Comprehensive Interfacial Analysis. *J. Mater. Chem. C* **2022**, *10* (10), 3929–3936.
- (37) Son, Y. J.; Kang, J. S.; Yoon, J.; Kim, J.; Jeong, J.; Kang, J.; Lee, M. J.; Park, H. S.; Sung, Y.-E. Influence of TiO2 Particle Size on Dye-Sensitized Solar Cells Employing an Organic Sensitizer and a Cobalt(III/II) Redox Electrolyte. *J. Phys. Chem. C* **2018**, *122* (13), 7051–7060.
- (38) Kim, H.-S.; Ko, S.-B.; Jang, I.-H.; Park, N.-G. Improvement of Mass Transport of the [Co(Bpy)3]II/IIIredox Couple by Controlling Nanostructure of TiO2 Films in Dye-Sensitized Solar Cells. *Chem. Commun.* **2011**, *47* (47), 12637–12639.
- (39) Hore, S.; Vetter, C.; Kern, R.; Smit, H.; Hinsch, A. Influence of Scattering Layers on Efficiency of Dye-Sensitized Solar Cells. *Sol. Energy Mater. Sol. Cells* **2006**, *90* (9), 1176–1188.
- (40) Deepak, T. G.; Anjusree, G. S.; Thomas, S.; Arun, T. A.; Nair, S. V.; Sreekumaran Nair, A. A Review on Materials for Light Scattering in Dye-Sensitized Solar Cells. *RSC Adv.* **2014**, *4* (34), 17615–17638.
- (41) Anderson, A. Y.; Barnes, P. R. F.; Durrant, J. R.; O'Regan, B. C. Quantifying Regeneration in Dye-Sensitized Solar Cells. *J. Phys. Chem.* C **2011**, *115* (5), 2439–2447.
- (42) Mishra, A.; Fischer, M. K. R.; Bäuerle, P. Metal-Free Organic Dyes for Dye-Sensitized Solar Cells: From Structure: Property Relationships to Design Rules. *Angew. Chem., Int. Ed.* **2009**, 48 (14), 2474–2499.
- (43) Urbani, M.; Grätzel, M.; Nazeeruddin, M. K.; Torres, T. Meso-Substituted Porphyrins for Dye-Sensitized Solar Cells. *Chem. Rev.* **2014**, *114* (24), 12330–12396.
- (44) Connelly, N. G.; Geiger, W. E. Chemical Redox Agents for Organometallic Chemistry. *Chem. Rev.* **1996**, *96* (2), 877–910.
- (45) Papageorgiou, N.; Athanassov, Y.; Armand, M.; Bonhoyte, P.; Pettersson, H.; Azam, A.; Grätzel, M. The Performance and Stability of Ambient Temperature Molten Salts for Solar Cell Applications. *J. Electrochem. Soc.* **1996**, *143* (10), 3099.
- (46) Papageorgiou, N.; Grätzel, M.; Infelta, P. P. On the Relevance of Mass Transport in Thin Layer Nanocrystalline Photoelectrochemical Solar Cells. *Sol. Energy Mater. Sol. Cells* **1996**, 44 (4), 405–438.
- (47) Kalaignan, G. P.; Kang, Y. S. A Review on Mass Transport in Dye-Sensitized Nanocrystalline Solar Cells. *J. Photochem. Photobiol. C Photochem. Rev.* **2006**, 7 (1), 17–22.
- (48) Bisquert, J.; Fabregat-Santiago, F. Impedance Spectroscopy: A General Introduction and Application to Dye-Sensitized Solar Cells. *Impedance Spectrosc* **2010**, 99.
- (49) Bredar, A. R. C.; Chown, A. L.; Burton, A. R.; Farnum, B. H. Electrochemical Impedance Spectroscopy of Metal Oxide Electrodes for Energy Applications. *ACS Appl. Energy Mater.* **2020**, 3 (1), 66–98.
- (50) Fackler, J. P.; Avdeef, A.; Fischer, R. G. Sulfur chelates. XVI. Chemical Properties of Oxidized Nickel(II) Dithiocarbamates. The X-Ray Crystal Structure of Tris(N,N-Di-n-Butyldithiocarbamato)-Nickel(IV) Bromide, NiC27 H54 N3 S6 Br. J. Am. Chem. Soc. 1973, 95 (3), 774–782.
- (51) Gardner, J. M.; Abrahamsson, M.; Farnum, B. H.; Meyer, G. J. Visible Light Generation of Iodine Atoms and I-I Bonds: Sensitized I-Oxidation and I3- Photodissociation. *J. Am. Chem. Soc.* **2009**, *131* (44), 16206–16214.
- (52) Gershgoren, E.; Banin, U.; Ruhman, S. Caging and Geminate Recombination Following Photolysis of Triiodide in Solution. *J. Phys. Chem. A* **1998**, *102* (1), 9–16.
- (53) Boschloo, G.; Häggman, L.; Hagfeldt, A. Quantification of the Effect of 4-Tert-Butylpyridine Addition to I-/I3- Redox Electrolytes in

- Dye-Sensitized Nanostructured TiO2 Solar Cells. J. Phys. Chem. B 2006, 110 (26), 13144-13150.
- (54) Raithel, A. L.; Meador, W. E.; Kim, T.-Y.; Staples, R. J.; Delcamp, J. H.; Hamann, T. W. Molecular Switch Cobalt Redox Shuttle with a Tunable Hexadentate Ligand. *J. Am. Chem. Soc.* **2023**, 145 (2), 1367–1377.
- (55) Rui, H.; Shen, J.; Yu, Z.; Li, L.; Han, H.; Sun, L. Stable Dye-Sensitized Solar Cells Based on Copper(II/I) Redox Mediators Bearing a Pentadentate Ligand. *Angew. Chem., Int. Ed.* **2021**, *60* (29), 16156–16163.
- (56) Fürer, S. O.; Milhuisen, R. A.; Kashif, M. K.; Raga, S. R.; Acharya, S. S.; Forsyth, C.; Liu, M.; Frazer, L.; Duffy, N. W.; Ohlin, C. A.; Funston, A. M.; Tachibana, Y.; Bach, U. The Performance-Determining Role of Lewis Bases in Dye-Sensitized Solar Cells Employing Copper-Bisphenanthroline Redox Mediators. *Adv. Energy Mater.* **2020**, *10* (37), 2002067.
- (57) Kannankutty, K.; Chen, C.-C.; Nguyen, V. S.; Lin, Y.-C.; Chou, H.-H.; Yeh, C.-Y.; Wei, T.-C. Tert-Butylpyridine Coordination with [Cu(Dmp)2]2+/+ Redox Couple and Its Connection to the Stability of the Dye-Sensitized Solar Cell. *ACS Appl. Mater. Interfaces* **2020**, *12* (5), 5812–5819.
- (58) Kavan, L.; Saygili, Y.; Freitag, M.; Zakeeruddin, S. M.; Hagfeldt, A.; Grätzel, M. Electrochemical Properties of Cu(II/I)-Based Redox Mediators for Dye-Sensitized Solar Cells. *Electrochim. Acta* **2017**, 227, 194–202.
- (59) Ndaleh, D.; Kaur, R.; Hogue, A.; Delcamp, J. H. Benzothiophene-Based Cross-Conjugated Organic Dyes for High-Photocurrent Dye-Sensitized Solar Cells with Photocurrents up to 27 mA/Cm2. ACS Appl. Energy Mater. 2023, 6 (20), 10376–10388.